Volume 17
Number 10
14 March 2025
Pages 5485-6186

Nanoscale

rsc.li/nanoscale

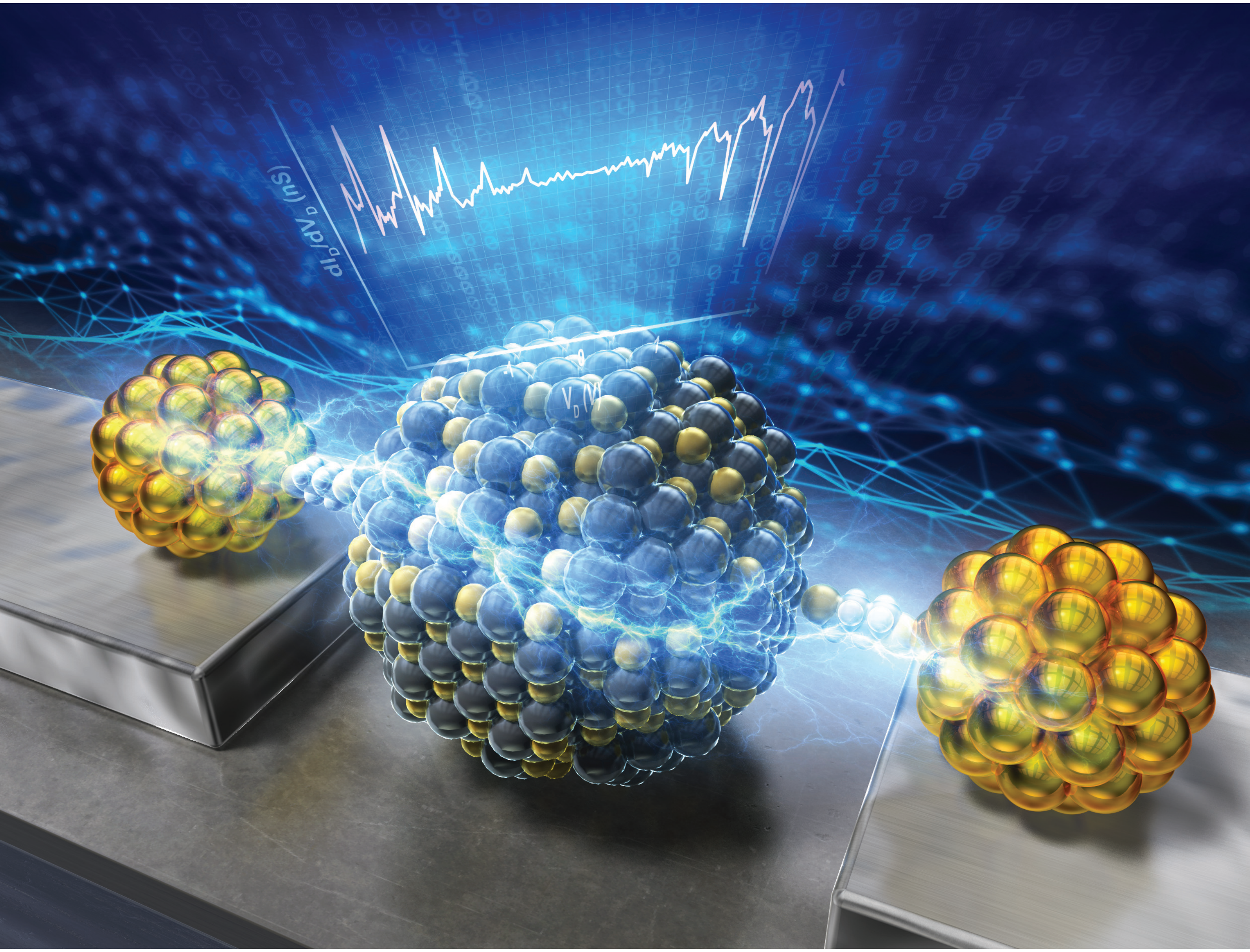

ISSN 2040-3372

COMMUNICATION
Satria Zulkarnaen Bisri, Yutaka Majima *et al.*
Molecularly-anchored single PbS quantum dots as resonant tunnelling transistors

Nanoscale

COMMUNICATION

View Article Online
View Journal | View Issue

Check for updates

Cite this: *Nanoscale*, 2025, **17**, 5672

Received 10th November 2024,
Accepted 12th January 2025

DOI: 10.1039/d4nr04703f

rsc.li/nanoscale

Molecularly-anchored single PbS quantum dots as resonant tunnelling transistors†

Retno Dwi Wulandari, [a,b,c] Dongbao Yin, [a] Ricky Dwi Septianto, [b,c] Seiichiro Izawa, [a] Yoshihiro Iwasa, [b] Satria Zulkarnaen Bisri *[b,c] and Yutaka Majima *[a]

The growing need for high-performance computing continues to drive improvement in circuit and device technologies, particularly with respect to speed and power efficiency. Device scaling remains the most effective strategy for meeting circuit performance requirements while reducing power consumption. Thanks to their solution processability, colloidal semiconductor quantum dots (QDs) are highly suitable for device miniaturisation as quantum information science platforms. Quantum mechanical effects must be carefully considered when designing nanometre-scale electronic devices (*i.e.*, transistors) that incorporate a single QD. Here, we demonstrate a resonant tunnelling transistor (RTT) based on a single lead sulfide (PbS) QD anchored by a bidentate ligand molecule attached to heteroepitaxial spherical Au/Pt nanogap electrodes. Five negative differential resistances (NDRs) were observed at both positive and negative drain voltages in output characteristics, which could be attributed to the formation of a double-barrier "quantum well" structure with the strong Fermi level pinning of the discrete energy level of the QD to one electrode. Furthermore, these NDRs could be tuned by applying a gate electric field, which will become one of the keys for enabling quantum and neuromorphic electronics. This demonstration of single PbS-QD-based RTTs paves the way for sub-10 nm solution-processable quantum electronic devices.

Introduction

In recent years, the continuous scaling of semiconductor device technologies to improve speed and power has been the primary focus in device manufacturing, and has led to ultimately scaled feature sizes. The latest generation of core processors used in many computers utilises a tiny (10 nm) fin-field effect transistor (Fin-FET)[1,2] technology, which works on the principle of a conventional FET. However, further shrinkage of the channel region in metal–oxide-semiconductor FET (MOSFETs) on bulk silicon substrates introduces short-channel effects, which challenges device performance by increasing leakage current and off-current.[3] On the other hand, these binary devices (which have dominated the electronic industry and link the natural property of devices to being in the ON or OFF state with two logic levels) provide the least possible information content per interconnect.[4] Multi-valued logic (MVL) has been considered to improve computation efficiency and reduce the power consumption of modern chips.[5] MVL is a non-binary-valued system in which more than two levels of information content are available. Consequently, MVLs enable higher information density, allowing logic functions to be performed with fewer logic gates and interconnects.

Negative differential resistance (NDR) is characterised by a decrease in drain current (I_D) while the drain voltage (V_D) increases. These NDR regions have been proposed to originate from resonant electron tunnelling through discrete energy levels in quantum well structures.[6–9] Recently, NDR effects in semiconductors have attracted significant interest in developing high-frequency oscillators, high-speed logic, and memory devices.[10–12] Importantly, multiple NDRs in resonant tunnelling transistors (RTTs) are particularly promising for proposed MVL applications due to their fast switching speed and the potential for device miniaturisation.[13,14] Furthermore, the tunnelling mechanism in RTTs is advantageous because, unlike various conventional FETs, RTTs are predicted to not suffer from short-channel effects due to their tunnelling mechanism.[15,16]

Recent advances in the synthesis and technologies of advanced materials have restarted the interest in driving progress in the MVL field, alongside the urgency to make these

---

[a] Materials and Structures Laboratory, Institute of Integrated Research, Institute of Science Tokyo, 4259 Nagatsuta-cho, Midori-ku, Yokohama, Kanagawa 226-8503, Japan. E-mail: majima@msl.titech.ac.jp

[b] RIKEN Center for Emergent Matter Science (CEMS), 2-1 Hirosawa, Wako, Saitama 351-0198, Japan

[c] Department of Applied Physics and Chemical Engineering, Tokyo University of Agriculture and Technology, 2-24-16 Nakacho, Koganei, Tokyo 184-8588, Japan. E-mail: satria-bisri@go.tuat.ac.jp

† Electronic supplementary information (ESI) available. See DOI: https://doi.org/10.1039/d4nr04703f

technologies practical. Among all emerging materials (that also include van der Waals (vdW), organics, and oxide materials), colloidal semiconductor quantum dots (QDs) are among the best candidates for realising MVL devices. The recent development of well-defined synthetic procedures for certain QD compounds, along with their low-cost fabrication, makes colloidal QDs highly suitable to support device miniaturisation through solution processing, thereby positioning them as ideal candidates for new platforms in quantum information science.[17,18]

Colloidal QDs possess quantum confinement effects, which leads to the quantisation of their discrete energy levels and bandgap tunability by size.[19,20] This quantum confinement effect is crucial for designing nanometre-scale electronic devices (*i.e.*, transistors) that involve a single QD.[21–23] The study of single colloidal QD devices has gained renewed attention in recent years due to their potential advanced electronic application. Recently, single PbS colloidal QDs have demonstrated significant advances, including the observation of single-electron transistor (SET) behaviour and even Kondo effects,[21] highlighting their versatility in exploring quantum phenomena at the nanoscale. Additionally, using our unique electroless Au plating (ELGP) method of heteroepitaxial-spherical (HS) Au/Pt nanogap electrodes, we recently reported the coexistence of resonant tunnelling current and single-electron tunnelling current on a single cadmium sulphide (CdS) colloidal QD SET.[24]

HS-Au/Pt nanogap electrodes have been fabricated by combining ELGP with electron beam lithography (EBL), resulting in a fabrication yield of 90% without any short circuit.[30–32] Au nanogap electrodes are commonly known to be thermally unstable owing to Rayleigh instability.[25,26] Therefore, we introduced Pt as the base material for source and drain electrodes, with a 10 nm linewidth, to achieve large gate capacitance.[27] Pt is a more suitable material because of its higher melting point and a surface diffusion coefficient that is 10^7 to 10^8 times smaller than that of Au.[28] We then established the fabrication process of an ELGP HS-Au/Pt nanogap on a Pt-based nanogap, allowing the heteroepitaxial growth of Au on initial polycrystal Pt nanogap electrodes to decrease and control the gap separation for single QD devices[29–31] (ESI Note 2†). Our ELGP is a unique method that enables the simultaneous fabrication of multiple nanogaps and precise control of the gap separation of nanogap electrodes.[30,31]

An essential strategy is a bottom–up approach to fabricating a high-quality single QD transistor based on the colloidal process that can be anchored between HS-Au/Pt nanogap electrodes. The HS-Au/Pt nanogap consists of one pair of Au spheres with small radii (<5 nm), so a single QD could be anchored using a thiol-based bidentate ligand to Au electrodes.[24,30]

The resonant tunnelling current coexists with the single-tunnelling electron tunnelling current on a single QD SET,[24] so the resonant tunnelling current flows through the quantised energy levels of the QD and depends on the number of electrons on the QD. This is beneficial for implementing MVL devices. Nevertheless, challenges related to the conceptual fabrication of MVL devices require radical solutions.

Here, we demonstrate multiple NDRs in RTTs utilising a single lead sulfide (PbS) colloidal QD as its fundamental building block. PbS QDs were chosen for their well-established synthetic process and large electron Bohr radius. This provides robust and stable quantum confinement at the given QD diameters, leading to the well-defined formation of discrete energy levels. To effectively anchor the single QD between the nanogap electrodes, self-assembled monolayers (SAMs) of 1,2-ethanedithiol (EDT) and 1,4-butanedithiol (BuDT) were formed on the surface of our HS-Au/Pt nanogap electrodes. These ligands are critical for creating a strong and stable anchor between the QD and electrode, which is essential for enabling Fermi-level pinning and enhancing resonant tunnelling, ultimately leading to the observation of NDR. We discussed the properties of single PbS QD transistors, focusing on the multiple NDR features and Coulomb oscillations observed with and without dithiol anchoring. The role of dithiol anchoring was analysed, particularly in how it may help pin the QD Fermi level to the electrode as the possible mechanism of RTT operations.

Results and discussion

Device structure

A schematic illustration of a fabricated RTT structure is shown in Fig. 1a. A single PbS QD was present between HS-Au/Pt nanogap electrodes. The landing of the PbS QD on the surface of the SiO_2/Si substrate allowed the 50 nm SiO_2 dielectric to function as the back-gate of the RTT. We utilised a QD of diameter 8.1 nm as the quantum island with a narrow bandgap of 0.66 eV and a large Bohr exciton radius of 18 nm (Note 1, ESI, and Fig. S1 and S2†).[33] This QD diameter has also been used to investigate the charge carrier transport in large-scale QD superlattice assemblies.[34]

Appropriate selection of dithiol anchor molecules enables us to realise high-performance RTT based on a single PbS QD. It should be noted that PbS colloidal QDs are protectively capped by long and insulating native oleic acid (OAc) ligands. Ligand exchange in the solid-state is the viable way to replace these native oleic acid ligands with the desired anchoring ones.[35] However, performing ligand exchange on the QD after it has landed between the nanogap electrode would be challenging due to the potential movement of the QDs during the exchange process.[36]

Therefore, we introduced a method that simultaneously exchanges the ligand and directly anchors the QD onto the HS-Au/Pt nanogap electrode. It was achieved by preparing EDT or BuDT SAM on the HS-Au/Pt nanogap electrode on which the QD will be anchored.[37,38] The stronger affinity of the thiol-based bidentate ligands to the surface of the PbS QD than of the OAc enables the attachment of the PbS QD and replacement of the OAc.[39–41] Consequently, the prepared nanogap separation should be designed to equal the sizes of the QD

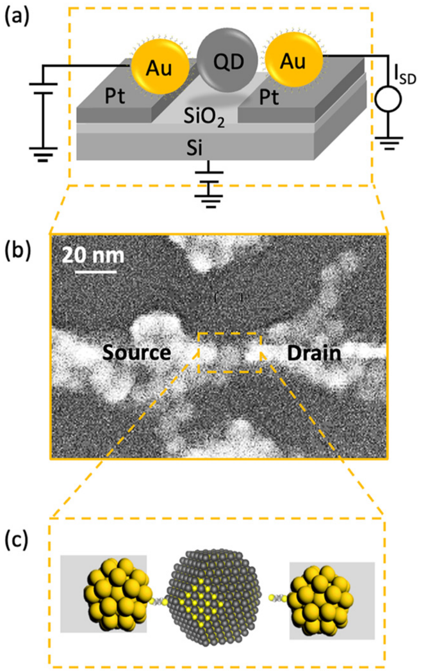

Fig. 1 Resonant tunnelling transistor of a single PbS colloidal quantum dot. (a) Structure of a PbS QD RTT (schematic). (b) SEM image of ELGP HS-Au/Pt nanogap electrodes separated by a gap of ~9 nm onto which PbS QDs (d ~8.1 nm) have been one side-chemisorbed. (c) Simplified illustration of the magnified RTT with the top-view perspective. 1,2-ethanedithiol (EDT) is chemically anchored the PbS QD core to a spherical Au electrode.

and the bidentate molecules. Fig. 1b shows the scanning electron microscope (SEM) image of the fabricated RTT with a PbS QD of 8.1 nm. The small gap between the QD and Au source electrode suggests anchoring by the alkane-dithiol molecule (in this case, EDT).

The two alkane-dithiol anchoring molecules with different chain lengths (BuDT and EDT) were expected to modulate the carrier transport of the RTT. The molecular lengths for EDT, BuDT, and OAc are 0.5 nm, 0.7 nm, and 2 nm, respectively, which change the distance between the QD and the Au electrode. Additionally, the ligand exchange process of oleic acid with thiol-based ligands alters the configurations of a single QD between the HS-Au/Pt nanogap electrode. The width of the tunnel barriers can be adjusted using these molecular ligands with different chain lengths, which varies the interaction between the discrete energy levels of QD and Au electrodes. The strong bonds between Au and the alkane-dithiol, as well as between the alkane-dithiol and the PbS QD, anchor the QD with the Au electrode, and Fermi-level pinning becomes strong by decreasing the chain length in the nanogap system.[42–45] This combination of HS-Au/Pt nanogap electrodes and molecular anchoring resulted in a yield of working RTT of 1.3%.

Negative differential resistance in transport measurements

Low-temperature transport measurements of the transistors were performed in a cryogenic probe station at 9 K. The robustness of the ELGP HS-Au/Pt nanogap electrode allows for the application of a relatively high electrical drain bias voltage (V_D) across the source and the drain electrodes, up to 3 V, without Au atom migration. To modulate the electronic state of the PbS QDs in the transistor, we utilised only the back-gate voltage through SiO_2 (50 nm). Fig. 2a shows the 9 K I_D–V_D characteristics of the PbS QD RTT, which used a 0.7 nm BuDT ligand under the application of different back-gate voltages (V_G) from −3.00 V to −2.72 V. This device exhibited decreases in its I_D as the V_D increased at some V_D regions, alongside a generally monotonous increase in I_D. Five negative differential resistance (NDR) phenomena were observed in the PbS QD RTT in both positive and negative V_D regions. We also measured the I_D–V_D characteristics under forward and backward sweeps (Fig. S4†). Even the peak and valley V_D changed slightly due to charge trapping around the QD; the same number (5) of NDR phenomena were observed on forward and backward sweeps. It should be noted that NDR phenomena are absent in conventional QD assembly FETs[34,36,39,41,46] and the recently reported single PbS QD SET.[21]

We then estimated the ratio of the current at the resonant tunnelling peak to that at the valley before the current started to increase again with voltage, commonly referred to as the peak-to-valley ratio (PVR). The latter is a widely used metric for measuring NDR performance. PVR values were calculated at five distinct NDR peaks as 1.32, 1.27, 1.35, 1.32, and 1.45 (Fig. S6†). Although smaller than that in single-molecule transistor-based[47] and molecular monolayer-based[48] NDR devices, which can achieve a PVR of over 30 and 100, respectively, to our knowledge, multiple (5) NDRs and this PVR value are the first ever reported for a single-QD RTT.

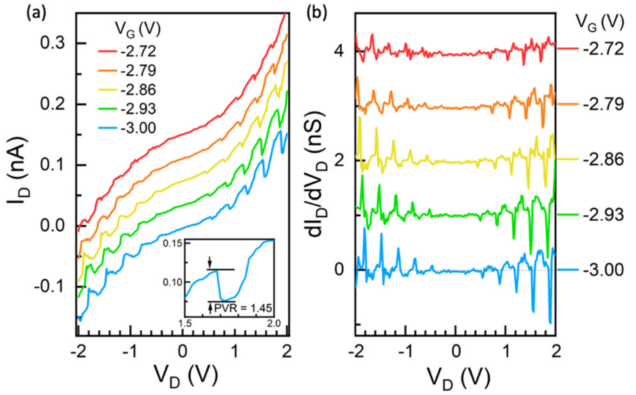

Fig. 2 Negative differential resistance (NDR) in a single PbS QD resonant tunnelling transistor. (a) The measured current–voltage (I_D–V_D) characteristics of a 1,4-butane dithiol (BuDT)-anchored PbS QD transistor at T = 9 K, taken at every 70 mV step of the back-gate voltage (V_G), showing multiple NDR peaks in both negative and positive drain voltage (V_D) regimes. (b) The corresponding dI_D/dV_D–V_D characteristics. The V_G dependence of differential conductance dI_D/dV_D was numerically calculated based on the experimental I_D–V_D characteristics, showing the electronic states of PbS QD. For clarity, the I_D–V_D and dI_D/dV_D–V_D characteristics are offset by 37.5 pA and 1 nS, respectively. Only the bottom curves at V_G = −3.0 V correspond to the actual scale.

Due to the capability to apply a large bias voltage ranging from −2 V to 2 V, we could observe multiple periods of NDR features in both positive and negative V_D regimes. Five NDR periods are available in both regimes, which can be used in five multi-logic states within this V_D range.

We plotted the differential conductance dI_D/dV_D of the QD device for different values of applied V_G to highlight the peaks and valleys of NDR behaviour (Fig. 2b). The origin of the observed NDR was fundamentally tied to the discrete energy levels in the PbS QD and the alignment of these energy levels with the Fermi levels of the source/drain electrodes. The nearly periodic peak-to-peak voltages of the NDRs (approximately 290–360 mV) reflected the interplay between Coulomb blockade effects and the degeneracy of the 1S level in the PbS QD.

Unlike Cd- or Hg-chalcogenides, which exhibit single degeneracy,[49] lead chalcogenides, such as PbS, have an intriguing band structure with the fundamental gap located at the L-point of the Brillouin zone.[50–52] Therefore, they have four-fold valley degeneracy. The characteristics of valley degeneracy of the compound can be translated into the multiplicity of the energy levels in single QD devices. This occurrence has been observed in single Si QD devices.[53–55]

Therefore, the PbS QD can lead to quantum-confined levels with a four-fold[34,41,56] higher multiplicity than materials like CdS QD. Eight electrons can occupy four-fold valley degeneracy. Our observation of five equally spaced resonances, corresponding to the sequential filling of the eight-fold degenerate electron level, confirmed the higher multiplicity of PbS energy levels. This high degeneracy allows for multiple NDR features as the voltage varies, reflecting the periodic alignment of these degenerate states with the electrode Fermi level, resulting in periodic NDR spacing. Our results on equally spaced peak-to-peak features are consistent with previous reports on another lead chalcogenide with four-fold degeneracy, specifically PbSe QDs.[57,58] Importantly, by using ELGP HS-Au/Pt nanogap electrodes, we could apply a broader voltage range, enabling us to access more resonance peaks.

In contrast to II–VI semiconductors, the effective masses of electrons and holes are nearly equal, leading to symmetric conduction and valence bands. The two lowest levels in this structure had S and P envelope symmetry, respectively. The measured tunnelling spectrum reflected the symmetric levels scheme (Fig. 2b and Fig. S5†).

The observation of NDRs in the measured I_D–V_D characteristics strongly indicated that this sample operated as an RTT. To highlight the reproducibility of these features, we presented similar NDR phenomena in another transistor (Note 4, ESI†), which exhibited well-pronounced multiple NDR properties in positive and negative V_D bias regimes (Fig. S7†), with PVR values of 1.39, 1.33, 1.29, 1.23, and 1.27 (Fig. S8†).

Replacing BuDT with shorter bidentate thiol ligands, such as EDT, could enhance the coupling between the Au electrodes and PbS QD. Notably, the measured I_D–V_D characteristics of these EDT-anchored devices also exhibited NDR properties in both positive and negative V_D regions (Fig. S9†). The differential conductance as a function of gate voltage also indicated the NDR feature, with a slight shift towards positive V_D as V_G decreased. A comparable shift in the NDR peaks was also observed in BuDT-anchored devices (Fig. 2b), confirming that both devices underwent effective gate modulation. The observations of NDR features in these two sets of RTTs demonstrated that pinning the QD Fermi level to the electrode using strong bonding between bidentate thiol molecules and Au was crucial for achieving resonant tunnelling transport.

Measurement of Coulomb oscillation in transport

Another feature of these RTTs was the observation of Coulomb oscillation in their I_D–V_G characteristics. Fig. 3a shows the BuDT-anchored QD RTT I_D as a function of the applied V_G. Instead of a monotonous increase in the I_D–V_G characteristics, we observed clear Coulomb oscillations. As shown in Fig. 2a, Coulomb blockade phenomena were not observed in I_D–V_D characteristics. However, Coulomb oscillation behaviours were observed. Each Coulomb oscillation peak indicated a change in the number of electrons in the PbS QD, with one electron tunnelling through different energy levels. The discrete energy levels of the QD and the well-defined double barrier tunnelling junction structure of the RTT allowed observation of these Coulomb oscillations. Over a V_G modulation range of 2.7 V (-5 V < V_G < -2.3 V), six Coulomb oscillation peaks were observed with a peak-to-peak V_G difference (ΔV_G) of ∼0.5 V. In addition to BuDT, we utilised the shorter dithiol ligand, EDT, as shown in Fig. 3b. Within the same range of applied V_G (2.7 V) on the EDT-anchored QD RTT, approximately six Coulomb oscillation peaks were observed, similar to the number seen in the BuDT-anchored QD RTT. This similarity could later be observed in the number of parallel lines in Fig. 4.

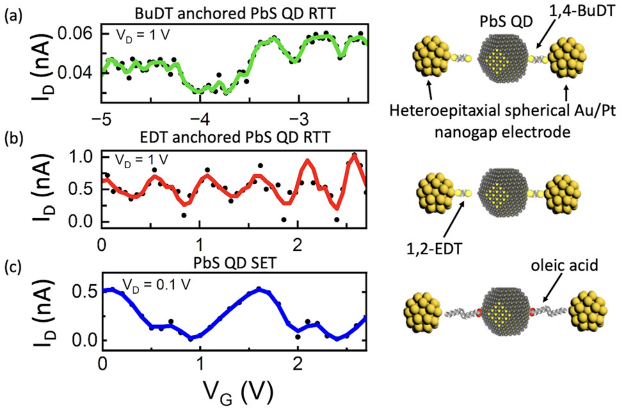

Fig. 3 Coulomb oscillations in different PbS QD transistors. The measured drain current–gate voltage (I_D–V_G) characteristics of PbS QDs transistor devices with different ligand molecules. The ligand molecules have different lengths (l) and relative permittivity (ε_r): (a) 1,4-butanedithiol (BuDT) (l = 0.7 nm and ε_r = 12), (b) 1,2-ethanedithiol (EDT) (l = 0.5 nm and ε_r = 12), and (c) the native oleic acid (l = 2 nm and ε_r = 2.85). In devices (a) and (b), each ligand molecule has two thiol end moieties, which are chemically anchored to PbS QD and Au one electrode. In contrast, in device (c), oleic acid molecules bind only to the PbS QD and are merely physisorbed between the HS-Au/Pt nanogap electrodes.

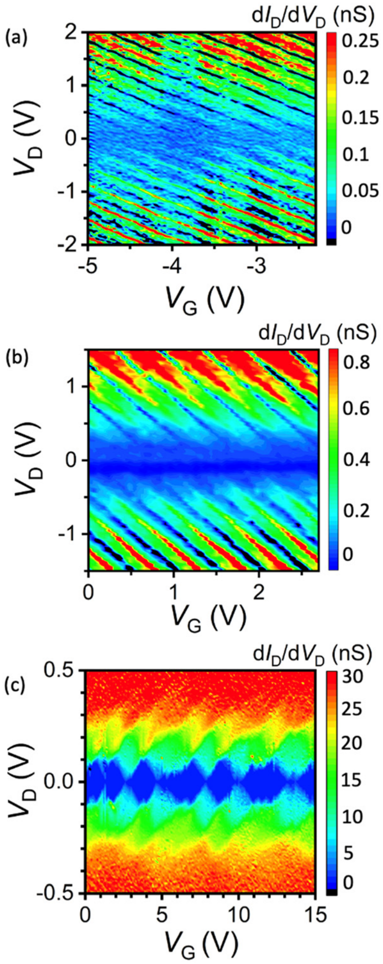

Fig. 4 2D dI_D/dV_D mapping of PbS QD transistors. Contour mapping stability diagrams were obtained by plotting colour maps of dI_D/dV_D as functions of V_D and V_G for (a) 1,4-Butanedithiol (BuDT)-anchored PbS QD RTT, (b) 1,2-ethanedithiol (EDT)-anchored PbS QD RTT, and (c) oleic acid-capped PbS QD SET. All measurements were carried out at T = 9 K.

In contrast, Fig. 3c shows the corresponding I_D–V_G transfer characteristics of PbS QD capped with molecules with carboxylic acid moieties, *i.e.*, oleic acid (OAc), which exhibited a much smaller number of Coulomb oscillations. Within the similar V_G range, only two peaks were observed, with a peak-to-peak V_G difference of approximately 1.5 V. A similar number of Coulomb oscillation peaks was reproducibly observed in another set of OAc-capped PbS QD devices (Fig. S10†).

The number of Coulomb oscillations directly determines the number of possible logic states that can be generated. A higher number of logic states can be achieved within the same V_G range if the spacing between oscillation peaks (ΔV_G) is smaller. In other words, a small ΔV_G is preferable for creating logic states.

Discussion

The 2D (V_D and V_G) differential conductance (dI_D/dV_D) plots, so-called "stability diagrams", provide a better representation of the electrical properties of the PbS QD RTTs and SETs. Fig. 4a shows the stability diagram of the BuDT-anchored PbS QD device. Although Coulomb diamonds were not observed, parallel conductance lines from the upper-left to lower-right were observed. In PbS QD RTTs, two tunnelling junctions were present between the HS-Au/Pt nanogap and PbS QD core. Coulomb blockade was not observed, implying the tunnelling resistance between the PbS QD core and the Au one electrode anchored by the BuDT was lower than the quantum resistance (h/e^2 (= 25.8 kΩ), h = Planck constant, e = unit charge).[59] With the total resistance of the BuDT-anchored PbS QD RTT exceeding 1 GΩ, the other tunnelling resistance was approximately equal to the total resistance of the PbS QD RTT. It suggests the Fermi energy levels of the PbS QD were pinned to that of the source or drain electrode at the BuDT-anchored tunnelling junction.

On the larger tunnelling junction side, either at the source or the drain electrodes, a resonant tunnelling current flowed when the Fermi level of the electrode aligned with the available pinned discrete energy levels of the QD. This alignment enhanced the tunnelling current, which appeared as parallel red conductance line features corresponding to the NDR peaks.

Meanwhile, parallel black lines ($dI_D/dV_D < 0$) were observed between these red parallel conductance lines, which corresponded to the NDR valleys. These valleys occur if the alignment between the Fermi level of the electrode and the pinned discrete energy level is disrupted.

The stability diagram also showed parallel red and black line patterns for the EDT-anchored PbS QD device, suggesting RTT operation (Fig. 4b). This device demonstrated wider conductance peak-to-peak V_G periods and higher conductance values than those of BuDT-anchored PbS QD.

The well-defined NDRs and Coulomb oscillations observed over a broad range of V_D and I_D in these bidentate ligand-anchored PbS QD transistors confirmed their operation as robust RTTs. This phenomenon also provided the most plausible explanation for the multiple parallel lines in the stability diagrams (Fig. 4a and b). The strong anchoring of PbS QDs to the HS-Au/Pt electrode using bidentate molecular ligands pins the QD Fermi energy level to the electrode. Consequently, the NDRs and Coulomb oscillations arise from quantum tunnelling and the quantised electron occupancy of the QD, which contain multiple resonant states or energy levels. Under specific bias conditions, tunnelling occurs through discrete energy levels within the quantum well structure of the device, producing NDRs and Coulomb oscillation regions.

These observations are challenging to interpret within the conventional framework of single-electron transistors (SETs). Studies on single PbS QD[21] or Si QD[53] transistors have predominantly utilised relatively long ligands to couple the QD with the electrodes, and Coulomb staircases without NDR have been observed in I_D–V_d characteristics as SET behaviour.

To investigate the dependence upon ligand length, we also attempted to fabricate a single PbS QD SET using longer ligands in conjunction with HS-Au/Pt nanogap electrodes. When native OAc capping ligands were retained without ligand exchange, the resulting PbS QD HS-Au/Pt nanogap device exhibited conventional SET behaviour. This finding aligns with prior studies, including recent work[21] that established the foundation of this field. The stability diagram (Fig. 4c) showed multiple Coulomb diamonds across the applied V_G range. Each diamond corresponded to a well-defined, quantised number of confined electrons in the PbS QD.

Notably, the greater number of the observed Coulomb diamonds in our study compared with that in earlier reports[21,60] could be attributed to the enhanced gate capacitance provided by the robust HS-Au/Pt nanogap electrodes. This configuration enabled the application of broader ranges of drain and gate voltage, extending the accessible operating regime of the device.

The difference between what has been observed in the devices utilising bidentate thiolate ligands and the native OAc ligand is striking. As the work function decayed exponentially against the distance, short bidentate thiolate ligands (EDT: l = 0.5 nm and BuDT: l = 0.7 nm)could bind strongly and enhance the overlap of the work functions between PbS QD and the Au electrode. On the contrary, the long native OAc ligand (2.0 nm) lacked the overlap of the work functions. Furthermore, the carboxylic acid moiety of the OAc has weaker bond strength to the PbS QD than thiolate ligands.[37] As a result, the PbS QD was "physisorbed" between the HS-Au/Pt nanogap electrodes. Consequently, a possible explanation of these differences is the overlap of the work functions through short and strong chemical anchoring that enhances Fermi-level pinning between the QD and the Au electrode, whereas a long OAc ligand inhibits Fermi-level pinning.

MVL aims to represent information using more than two binary states. Incorporating multiple NDR features allows for the efficient processing of a broader range of logic states, enabling more information to be carried per signal. This leads to increased data density and computational capability. Moreover, multiple NDRs in RTTs provide multiple logic states within a single device, potentially reducing the overall number of transistors and power consumption in the MVL system.[61] Therefore, the pronounced multiple (5) NDR behaviour observed in our single PbS QD transistor directly supports its potential for MVL logic circuits, high-frequency oscillators, and advanced memory applications.

In addition, the NDR features observed in our devices may be relevant to memristive behaviour. Studies have demonstrated that PbS QDs exhibit promising resistive switching properties and can be utilised for data storage and computing applications.[62,63] In those studies, the self-assembly of PbS QDs played a critical part in enabling memristor behaviour and enhancing the uniformity and performance of resistive switching devices. Similarly, the NDR behaviour in our device could serve as a foundation for multi-level memory devices or neuromorphic computing systems.

While we recognise that the current PVR observed in our device is relatively small, posing challenges for achieving practical MVL functionality, our study provides a foundation for further exploration of MVL concepts using NDR features in RTTs. The presence of multiple NDR peaks indicates a promising potential for MVL technology. Further optimisation, such as using a much smaller QD size or exploring alternative QD materials, might help achieve higher PVR. Additionally, the unique combination of resonant tunnelling and Coulomb oscillations demonstrated in our devices further distinguishes them from prior studies, which were largely limited to observing Coulomb blockade phenomena. These results suggest that our approach broadens the functionality of single QD transistors but also positions them as a versatile platform for integrating QDs into practical MVL architectures. Such versatility is especially valuable for next-generation nanoelectronics, where high-speed and low-power requirements are paramount.

Conclusions

In conclusion, we have demonstrated robust solution-processable RTTs based on molecularly anchored single colloidal PbS QDs and HS-Au/Pt nanogap electrodes as promising pathways for developing MVL devices and possibly neuromorphic devices.

The type of ligand molecules strongly influenced the transport characteristics of the single PbS QD devices. Due to the strong Fermi level pinning between the QD and the Au electrode, short chemical anchoring of the QD using bidentate thiol ligands was the key to realising RTTs demonstrating clear NDRs and Coulomb oscillation behaviours, making them suitable for future MVL operations. The observed multiple NDR occurrences arose from the inherent properties of the used semiconducting colloidal PbS QDs, specifically their high degeneracy. In contrast, the absence of the overlap of the work functions on the long native OAc ligand led to conventional SET operation with well-defined Coulomb diamonds. The robustness and controllability of the RTT and SET operations based on single colloidal QD and HS-Au/Pt nanogap electrodes could pave the way for the future development of solution-processable MVL devices for quantum and neuromorphic electronics.

Experimental

Materials

High-quality PbS QDs were tested and procured from Quantum Solutions (**https://www.quantum-solutions.com**) following customisation of the synthetic protocol. PbS QDs of diameter 8.1 nm were used due to their superior assembly properties.[34] Transmission electron microscopy (TEM) images of PbS QDs were obtained using a JEM-1230 apparatus (JEOL) operating at 80 kV. Before TEM measurement, the prepared QD assembly on the TEM grid was baked at 100 °C for 1 h in a nitrogen glovebox. 1,2-ethanedithiol (EDT), 1,4-butanedithiol (BuDT), and acetonitrile (anhydrous, 99%) were procured from MilliporeSigma as ligands and solvent, and were stored within nitrogen gloveboxes. Iodide tincture, L (+)-ascorbic acid, and

Au sheets (99.99%) were procured to prepare the ELGP solution (ESI Note 2†). Deionised water (18.1 MΩ) was prepared and used. A highly doped Si wafer with 50 nm of thermally grown SiO_2 was used as the device substrate, serving as the bottom gate structure.

Preparation of ELGP HS-Au/Pt nanogap electrodes

HS-Au/Pt nanogap electrodes were prepared following established fabrication protocols.[29,30] Ultrafine Pt-based nanogap electrodes were patterned on SiO_2/Si substrates using electron beam lithography (EBL) using the ELS-7500EX system (Elionix). After developing the EBL resist, 3 nm of Ti and 10 nm of Pt film were deposited using an e-beam (EB) evaporator (ANELVA; Canon). Precise ultrafine Pt-based nanogap electrodes were obtained following the resist lift-off process (Fig. S3a†). We employed electroless gold plating (ELGP)[30,31,64] on the formed Pt nanogap electrodes to further decrease and control the gap separation of the HS-Au/Pt nanogap electrodes with one pair of small Au spheres (radii < 5 nm). The initial ultrafine Pt-based nanogap electrodes were cleaned using an acetone/ethanol mixture and dry nitrogen flow, followed by UV-ozone cleaning to remove residual organic contaminants or resist. To prepare the ELGP solution (ESI Note 2†), an Au sheet (99.99%, 65 mg) was dissolved in 3 mL of iodine tincture (I_2 and KI in ethanol). As a reducing agent, L(+)-ascorbic acid was added to the saturation limit. Immersing the cleaned Pt nanogap electrodes into a diluted ELGP solution in 8 mL of DI water allowed the heteroepitaxial spherical growth of Au at the surface of the Pt nanogap. The electroless Au plating process was stopped by rinsing the nanogap electrode using DI water and an acetone/ethanol mixture. The ELGP produced robust nanogap electrodes with the desired gap separation for a single QD device platform (Fig. S3b†). Morphological and structural analyses of the nanogap electrode were carried out using field-emission scanning electron microscopy (FE-SEM) employing the Regulus 8230 setup (Hitachi).

Preparation of a single QD device

The PbS QD was anchored by molecular capturing of the QD to the HS-Au/Pt nanogap electrodes. Such molecular capture relies on the stronger interaction of the thiol moieties of the bidentate ligands on the QD surface than the carboxylic acid moieties of the native insulating oleic acid ligands. Before casting the PbS QD, the ELGP HS-Au/Pt nanogap electrodes were immersed in 1 M of anchoring ligand solution in acetonitrile to form the bidentate self-assembled monolayer (SAM). The ligand solution consisted of either 1,4-butanedithiol (BuDT, $C_4H_{10}S_2$) or 1,2-ethanedithiol (EDT, $C_2H_6S_2$). The substrate immersion ran for 24 h. One thiol moiety would bind coordinatingly[45] to the spherical Au surface through a self-assembly process, leaving the other thiol moieties “dangling”. A coordinate bond was a typical Au–S covalent bond formed by sharing one pair of electrons, and both arose from the same atom. Due to thiol selectivity, bidentate thiol ligands would not attach to the SiO_2 surface. After drying the substrate (90 °C, 1 h), these treated nanogap samples were immersed (24 h) into a dilute hexane solution of PbS QDs of 8.1 nm in diameter, still capped by oleic acid. Upon landing on the treated nanogap electrode, the QD selectively released the oleic acid molecule to get captured by the dangling thiol moieties of the bidentate ligands on the nanogap electrode. Afterwards, methanol was used to rinse the samples to remove excess PbS QDs, unattached ligands, and released oleic acid. The samples were also baked at 90 °C (1 h) to remove excess solvents. Through this protocol, the PbS QD was anchored coordinatingly by the bidentate thiol ligands to the HS-Au/Pt nanogap electrode, with the bidentate ligand pinning the discrete energy level of PbS QD. It should be noted that all steps of HS-Au/Pt nanogap electrode treatment and the introduction of the colloidal QDs were conducted within a dry N_2-glovebox because both the bidentate ligands and the electronic properties of the PbS QDs are sensitive to oxygen and moisture.

Measurement of electrical transport

The measurement of electrical transport was performed in dark, cold (9 K), and vacuum conditions ($\sim 10^{-5}$ Pa) in a helium-refrigerated probe station (GRAIL10-LOGOS01S; Nagase) connected to a semiconductor parameter analyser (B1500A; Keysight) equipped with high-resolution source measure unit (HRSMU). We introduced the sample into the top-loading cryostat system (<5 min) after we broke the inert gas-sealed bag to minimize the potential for oxygen and moisture exposure. We started the characterization after thawing the sample at a high vacuum for 2 h to ensure the removal of oxygen or moisture adsorbates.[65,66] The experimental differential conductance dI_D/dV_D was numerically calculated based on the experimental I_D–V_D characteristics. Contour mapping stability diagrams were plotted by combining the measured drain current I_D as a function of V_D and V_G.

Author contributions

Y. M. and S. Z. B. conceived the research. R. D. W. performed most of the device preparations and the transport measurements. R. D. S. helped in the pre-processing of PbS quantum dots. R. D. W. and D. Y prepared heteroepitaxial spherical Au/Pt nanogap electrodes. R. D. W., S. I., Y. I., S. Z. B., and Y. M. analysed and discussed the experimental data. R. D. W., Y. I., S. Z. B., and Y. M. wrote the manuscript with inputs from the other co-authors.

Data availability

Detailed material and electrode characterisations are shown in the ESI†: Molecularly anchored single PbS QD RTT.

Conflicts of interest

The authors declare no conflicts of interest.

Acknowledgements

This research was partly supported by CREST from the Japan Science and Technology Agency (JST) (JPMJCR22B4) (Y. M.), Grant-in-Aid for Scientific Research (C) (JP21K04815) (S. Z. B.), Scientific Research (S) (JP19H05602) (Y. I.) from the Japan Society for the Promotion of Science (JSPS), and Data Creation and Utilization Type Material Research and Development from Ministry of Education, Culture, Sports, Science and Technology (MEXT) (JPMXP1122683430) (Y. M.). Technical supports from M. Miyakawa and I. Shimada (Institute of Science Tokyo) are greatly appreciated.

References

1 M. L. Chen, X. Sun, H. Liu, H. Wang, Q. Zhu, S. Wang, H. Du, B. Dong, J. Zhang, Y. Sun, S. Qiu, T. Alava, S. Liu, D. M. Sun and Z. Han, *Nat. Commun.*, 2020, **11**, 1205.
2 J. Anderson, Y. He, B. Bahr and D. Weinstein, *Nat. Electron.*, 2022, **5**, 611–619.
3 A. Mallik and A. Chattopadhyay, *IEEE Trans. Electron Devices*, 2012, **59**, 277–282.
4 S. L. Hurst, *IEEE Trans. Comput.*, 1984, **33**, 12.
5 M. Andreev, S. Seo, K. S. Jung and J. H. Park, *Adv. Mater.*, 2022, **34**, 2108830.
6 J. Appenzeller, Y. M. Lin, J. Knoch and P. Avouris, *Phys. Rev. Lett.*, 2004, **93**, 196805.
7 Q. Zhang, W. Zhao and A. Seabaugh, *IEEE Electron Device Lett.*, 2006, **27**, 297–300.
8 W. Y. Choi, B. G. Park, J. D. Lee and T. J. K. Liu, *IEEE Electron Device Lett.*, 2007, **28**, 743–745.
9 Y. Khatami and K. Banerjee, *IEEE Trans. Electron Devices*, 2009, **56**, 2752–2761.
10 T. Sugaya, K. Y. Jang, C. K. Hahn, M. Ogura, K. Komori, A. Shinoda and K. Yonei, *J. Appl. Phys.*, 2005, **97**, 034507.
11 X. Xiong, M. Huang, B. Hu, X. Li, F. Liu, S. Li, M. Tian, T. Li, J. Song and Y. Wu, *Nat. Electron.*, 2020, **3**, 106–112.
12 G. A. Gibson, *Adv. Funct. Mater.*, 2018, **28**, 1704175.
13 K. J. Gan, J. J. Lu, W. K. Yeh, Y. H. Chen and Y. W. Chen, *Eng. Sci. Tech. Int. J.*, 2016, **19**, 888–893.
14 P. Mazumder, S. Kulkarni, M. Bhattacharya, J. P. Sun and G. I. Haddad, *Proc. IEEE*, 1998, **86**, 664–686.
15 A. S. Berhulst, W. G. Vandenberghe, K. Maex and G. Groeseneken, *Appl. Phys. Lett.*, 2007, **91**, 053102.
16 Y. R. Jhan, Y. C. Wu, H. Y. Lin and M. F. Hung, *Appl. Phys. Lett.*, 2013, **103**, 053118.
17 C. R. Kagan, L. C. Bassett, C. B. Murray and S. M. Thompson, *Chem. Rev.*, 2021, **121**, 3186–3233.
18 J. Almutlaq, Y. Liu, W. J. Mir, R. P. Sabatini, D. Englund, O. M. Bakr and H. Sargent, *Nat. Nanotechnol.*, 2024, **19**, 1091–1100.
19 A. I. Ekimov and A. A. Onushchenko, *J. Exp. Theor. Phys. Lett.*, 1981, **34**, 345–349.
20 M. A. Reed, J. N. Randall, R. J. Aggarwal, R. J. Matyi, T. M. Moore and A. E. Wetsel, *Phys. Rev. Lett.*, 1988, **60**, 535–537.
21 K. Shibata, M. Yoshida, K. Hirakawa, T. Otsuka, S. Z. Bisri and Y. Iwasa, *Nat. Commun.*, 2023, **14**, 7486.
22 D. L. Klein, R. Roth, A. K. L. Lim, A. P. Alivisatos and P. L. McEuen, *Nature*, 1997, **389**, 699–701.
23 M. Zdrojek, M. J. Esplandiu, A. Barreiro and A. Bachtold, *Phys. Rev. Lett.*, 2009, **102**, 226804.
24 G. Ohkatsu, T. Nishinobo, M. Saruyama, T. Teranishi and Y. Majima, *Nanoscale Adv.*, 2024, **6**, 4346–4351.
25 F. A. Nichols, *J. Mater. Sci.*, 1976, **11**, 1077–1082.
26 S. Karim, M. E. Toimil-Molares, A. G. Balogh, W. Ensinger, T. W. Cornelius, E. U. Khan and R. Neumann, *Nanotechnology*, 2006, **17**, 5954–5959.
27 M. Rauber, F. Muench, M. E. Toimil-Molares and W. Ensinger, *Nanotechnology*, 2012, **23**, 475710.
28 C. Alonso, R. C. Salvarezza, J. M. Vara and A. J. Arvia, *J. Electrochem. Soc.*, 1990, **137**, 2161.
29 Y. Y. Choi, T. Teranishi and Y. Majima, *Appl. Phys. Express*, 2019, **12**, 025002.
30 Y. Y. Choi, A. Kwon and Y. Majima, *Appl. Phys. Express*, 2019, **12**, 125003.
31 Y. Yasutake, K. Kono, M. Kanahera, T. Teranishi, M. R. Buitelaar, C. G. Smith and Y. Majima, *Appl. Phys. Lett.*, 2007, **91**, 203107.
32 C. S. Ah, Y. J. Yun, J. S. Lee, H. J. Park, D. H. Ha and W. S. Yun, *Appl. Phys. Lett.*, 2006, **88**, 133116.
33 S. Jiao, J. Wang, Q. Shen, Y. Li and X. Zhong, *J. Mater. Chem. A*, 2016, **4**, 7214–7221.
34 R. D. Septianto, R. Miranti, T. Kikitsu, T. Hikima, S. Hashizume, N. Matsushita, Y. Iwasa and S. Z. Bisri, *Nat. Commun.*, 2023, **14**, 2670.
35 S. Z. Bisri, C. Piliego, M. Yarema, W. Heiss and M. A. Loi, *Adv. Mater.*, 2013, **25**, 4309–4314.
36 R. D. Septianto, L. Liu, F. Iskandar, N. Matsushita, Y. Iwasa and S. Z. Bisri, *NPG Asia Mater.*, 2020, **12**, 33.
37 B. Kim, S. H. Choi, X. Y. Zhu and C. D. Frisbie, *J. Am. Chem. Soc.*, 2011, **133**, 19864–19877.
38 L. Yuan, C. Franco, N. Crivillers, M. Mas-Torrent, L. Cao, C. S. S. Sangeeth, C. Rovira, J. Veciana and C. A. Nijhuis, *Nat. Commun.*, 2016, **7**, 12066.
39 L. Liu, S. Z. Bisri, Y. Ishida, T. Aida and Y. Iwasa, *Nanoscale*, 2019, **11**, 20467–20474.
40 L. Liu, S. Z. Bisri, Y. Ishida, D. Hashizume, T. Aida and Y. Iwasa, *ACS Appl. Nano. Mater.*, 2018, **1**, 5217–5225.
41 L. Liu, R. D. Septianto, S. Z. Bisri, Y. Ishida, T. Aida and Y. Iwasa, *Nanoscale*, 2021, **13**, 14001–14007.
42 H. Ren, G. Zhang, N. Lin, L. Deng, Y. Luo and F. Huang, *Phys. Chem. Chem. Phys.*, 2016, **18**, 26586–26594.
43 S. Koley and S. Chakrabarti, *Chem. – Eur. J.*, 2018, **24**, 5876–5882.
44 N. Crivillers, M. Paradinas, M. Mas-Torrent, S. T. Bromley, C. Rovira, C. Ocal and J. Veciana, *Chem. Commun.*, 2011, **47**, 4664–4666.
45 R. T. Tung, *Phys. Rev. Lett.*, 2000, **84**, 6078–6081.

46 J. M. Fruhman, H. P. A. G. Astier, B. Ehrler, M. L. Bohm, L. F. L. Eyre, P. R. Kidambi, U. Sassi, D. D. Fazio, J. P. Griffiths, A. J. Robson, B. J. Robinson, S. Hofmann, A. C. Ferrari and C. J. B. Ford, *Nat. Commun.*, 2021, **12**, 4037.

47 K. Garg, C. Majumder, S. K. Gupta, D. K. Aswal, S. K. Nayak and S. Chattopadhyay, *RSC Adv.*, 2015, **5**, 50234–50244.

48 D. Yin, M. Furushima, E. Tsuchihata, S. Izawa, T. Ono, R. Shintani and Y. Majima, *Adv. Electron. Mater.*, 2024, **10**, 2400390.

49 X. Lan, M. Chen, M. H. Hudson, V. Kamysbayev, Y. Wang, P. Guyot-sionnest and D. V. Talapin, *Nat. Matter.*, 2020, **19**, 323–329.

50 G. Allan and C. Delerue, *Phys. Rev. B:Condens. Matter Mater. Phys.*, 2004, **70**, 245321.

51 P. Liljeroth, P. A. Zeijlmans van Emmichoven, S. G. Hickey, H. Weller, B. Grandidier, G. Allan and D. Vanmaekelbergh, *Phys. Rev. Lett.*, 2005, **95**, 086801.

52 F. W. Wise, *Acc. Chem. Res.*, 2000, **33**, 773.

53 B. Zaknoon, G. Bahir, C. Saguy, R. Edrei, A. Hoffman, R. A. Rao, R. Muralidhar and K. Chang, *Nano Lett.*, 2008, **8**, 1689–1694.

54 R. C. C. Leon, C. H. Yang, J. C. C. Hwang, J. C. Lemyre, T. Tanttu, W. Huang, K. W. Chan, K. Y. Tam, F. E. Hudson, K. M. Itoh, A. Morello, A. Laucht, M. Pioro-Ladrière, A. Saraiva and A. S. Dzurak, *Nat. Commun.*, 2020, **11**, 797.

55 M. Fuechsle, S. Mahapatra, F. A. Zwanenburg, M. Friesen, M. A. Eriksson and M. Y. Simmons, *Nat. Nanotechnol.*, 2010, **5**, 502–505.

56 I. Kang and F. W. Wise, *J. Opt. Soc. Am. B*, 1997, **14**, 1632–1646.

57 P. Liljeroth, L. Jdira, K. Overgaag, B. Grandidier, S. Speller and D. Vanmaekelbergh, *Phys. Chem. Chem. Phys.*, 2006, **8**, 3845–3850.

58 V. Notot, W. Walravens, M. Berthe, N. Peric, A. Addad, X. Wallart, C. Delerue, Z. Hens, B. Grandidier and L. Biadala, *ACS Nano*, 2022, **16**, 3081–3091.

59 D. V. Averin and K. K. Likharev, in *Mesoscopic Phenomena in Solids*, ed. B. L. Altshuler, P. A. Lee and R. A. Webb, Elsevier, Amsterdam, 1991.

60 A. Ismael, X. Wang, A. Al-Jobory, S. Ning, T. Alotaibi, B. Alanazi, H. Althobaiti, J. Wang, N. Wei, C. J. B. Ford and C. J. Lambert, *J. Mater. Chem. C*, 2024, **12**, 14004.

61 L. Lee, J. Hwang, J. W. Jung, J. Kim, H. I. Lee, S. Heo, M. Yoon, S. Choi, N. V. Long, J. Park, J. W. Jeong, J. Kim, K. R. Kim, D. W. Kim, S. Im, B. H. Lee, K. Cho and M. M. Sung, *Nat. Commun.*, 2019, **10**, 1998.

62 X. Yan, Y. Pei, H. Chen, J. Zhao, Z. Zhou, H. Wang, L. Zhang, J. Wang, X. Li, C. Qin, G. Wang, Z. Xiao, Q. Zhao, K. Wang, H. Li, D. Ren, Q. Liu, H. Zhou, J. Chen and P. Zhou, *Adv. Mater.*, 2019, **31**, 1805284.

63 Y. Pei, L. Yan, Z. Wu, J. Lu, J. Zhao, J. Chen, Q. Liu and X. Yan, *ACS Nano*, 2021, **15**, 17319–17326.

64 V. V. M. Serdio, T. Muraki, S. Takeshita, S. D. E. Hurtado, S. Kano, T. Teranishi and Y. Majima, *RSC Adv.*, 2015, **5**, 22160–22167.

65 D. M. Balazs, M. I. Nugraha, S. Z. Bisri, M. Sytnyk, W. Heiss and M. A. Loi, *Appl. Phys. Lett.*, 2014, **104**, 112104.

66 Y. Azuma, Y. Onuma, M. Sakamoto, T. Teranishi and Y. Majima, *Nanoscale*, 2016, **8**, 4720–4726.